NASA TECHNICAL MEMORANDUM

NASA TM X-71635

ION AND ELECTRON TEMPERATURES IN THE SUMMA MIRROR DEVICE BY EMISSION SPECTROSCOPY

by R. W. Patch, D. E. Voss, J. J. Reinmann,
and A. Snyder
Lewis Research Center
Cleveland, Ohio 44135
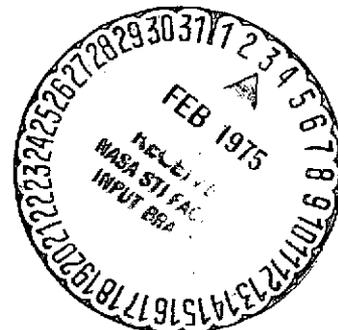
ION AND ELECTRON TEMPERATURES IN THE SUMMA MIRROR

DEVICE BY EMISSION SPECTROSCOPY

by R. W. Patch, D. E. Voss, J. J. Reinmann, and A. Snyder

Lewis Research Center

SUMMARY

Ion temperatures were obtained in the SUMMA mirror device by observing the Doppler-broadened charge-exchange component of the 667.8 and 587.6 nanometer He lines in He plasma and the H_α and H_β lines in H_2 plasma. The second moment of the line profiles was used as the parameter to determine ion temperature. Corrections for magnetic splitting, fine structure, monochromator slit function, and variation in charge-exchange cross section with energy are derived and included. Even for constant cross section, no magnetic splitting nor fine structure, and infinitely narrow slit function, the line profile is not Gaussian, because the excitation results from a change-exchange process. Comparison is made with temperatures from a neutral particle analyzer. Electron temperatures were measured by the line ratio method for the corona model and were always much less than the ion temperatures. Correlations of ion and electron temperatures with plasma parameters are given.

INTRODUCTION

The purpose of the present work was to measure ion and electron temperatures and ion drift in the superconducting magnetic mirror apparatus (SUMMA) at NASA Lewis Research Center. The heart of this facility is a steady-state magnetic-mirror device with crossed $\vec{\mathscr{E}}$ and $\vec{B}$ fields and superconducting magnets with the capability of producing a maximum midplane field of 4.9 tesla. The crossed $\vec{\mathscr{E}}$ and $\vec{B}$ fields cause the free electrons and ions of the plasma to drift azimuthally with approximately the same velocity, corresponding to an ion drift energy of as much as several kilovolts. In addition, it appears that turbulence occurs which results in ion heating (ref. 1). The ion temperatures in such devices are almost always many times the electron temperatures. The SUMMA facility is unique in that it has the highest design field strength for its bore size of any existing superconducting magnet device.

Ion and electron temperatures and ion drift were measured by emission spectroscopy in the optical region from 412.1 to 728.1 nanometer wavelength. The ion temperatures were determined from the width of the charge-exchange neutral components of atomic spectral lines. The methods used in this spectroscopic determination of ion temperature and the comparison of these temperatures with those determined in charge-exchange neutral detection is the principal subject of this report. An indication of the ion drift was obtained from the shift of the charge-exchange neu-

tral component of a spectral line relative to the narrow component associated with low energy neutral background particles. The electron temperature was found by taking ratios of intensities of spectral lines of helium and assuming a corona plasma model.

Little previous work has been done on charge-exchange neutral Doppler broadening, which was first noted in aurora borealis. Recently Alexeff, et al. (ref. 2) observed the phenomenon in deuterium Balmer-α, -β, and -γ spectra from the turbulently heated plasma of the mirror device Burnout V and observed that ". . . the most difficult problem here is that of appropriate unfolding of the line profile" (presumably in the presence of the narrow component and the slit function of the monochromator). Hess (ref. 3) used charge-exchange neutral spectra to find the velocity distribution of a hot plasma beam from an r.f.-heated high-density plasma source. Sigman and Reinmann (ref. 4) observed a charge-exchange component of H_β in a crossed-field mirror device.

Much previous work has been done on determining free electron temperature from He line intensity ratios assuming a corona model. A review has been given by Sovie (ref. 5). Some high density effects have been discussed by Sovie in a later paper (ref. 6). The most successful applications of the method have been made by Latimer, Mills, and Day (ref. 7) and Roth, Richardson, and Gerdin (refs. 8 and 9).

Some previous spectroscopic measurements of ion and electron temperature and ion drift in SUMMA were made by Reinmann, Lauver, Patch, Posta, Snyder, and Englert (ref. 10) with a different electrode configuration. In the present work, the anodes and floating shields were changed to water-cooled copper, and the spectroscopic techniques were modified. The ion temperatures were obtained from stronger lines with no anomalies and less interference and were corrected for magnetic splitting, fine structure (where present), monochromator slit function, and variation of charge-exchange cross section with energy. The ion drifts were obtained by taking averages of wavelength sweeps in both directions. The relative intensity calibration used in finding electron temperatures was improved.

The scope of the present work was, nevertheless, somewhat restricted. No Abel inversions are included because the small viewing ports did not allow vertical scanning of enough of the plasma. Nor was an inversion method available for charge-exchange neutral spectra at specific wavelengths. Transit time and high-density effects were not included. These and other effects are the subject of continuing research.

Results are reported for pure helium 4 and pure hydrogen plasmas. Also, a mixture of 90 percent by volume H_2 and 10 percent He was used to measure electron temperatures from He line ratios. It is presumed that these measurements approximate the electron temperature in pure hydrogen plasmas.

The authors are greatly indebted to Dr. Norman Tolk of Bell Telephone Laboratories for measuring the ratio of excitation cross sections

APPARATUS

Magnet Facility

The SUMMA facility (ref. 11) includes four solenoidal magnets of which the inboard two were used for the present work (see fig. 1). The details of the magnet system have already been reported elsewhere (refs. 10, 12, and 13). The two inboard magnets alone produce maximum fields of 5.2 and 3.5 tesla at the mirrors and midplane, respectively.

Plasma Test Section

A schematic view of the plasma test section is shown in figure 1. The discharge chamber is a cylinder 3.75 meters in length and 36.6 centimeters in diameter made from 304 stainless steel. A 10-inch diffusion pump at each end of the test section pumps the system to a base pressure of 5×10^{-7} torr. The large center port on one side was used for a neutral particle analyzer while the opposite port was used for spectroscopic observations.

Electrode Assembly

The electrode arrangement is also shown schematically in figure 1. More detail is shown in figure 2. Gas is introduced through the uncooled tungsten 12.7 millimeter-diameter cathodes to produce a hollow-cathode discharge. The water-cooled copper anode rings have 29 and 51 millimeter inside and outside diameters, respectively. They are electrically grounded to the test section walls. The electrically floating shield protects a cathode holder from heavy particle bombardment and helps inhibit arcing from the cathode holder to the anodes. The shield was constructed of copper and cooled by water. The anodes and cathodes are connected in parallel to a single d.c. power supply.

Spectroscopic Diagnostic Equipment

The apparatus for emission spectroscopy is shown in figure 3. It was located at the magnetic midplane with the line-of-sight always in the midplane. The vertical centerplane of the test section was focused on the entrance slit of the monochromator by means of a lens. Between the lens and the entrance slit, the beam was rotated 90° by means of a beam rotator consisting of totally reflecting prisms and mirrors. A stop was provided to reduce the vertical height of the beam. With this arrange-

ment, the area of the vertical centerplane viewed by the spectrometer was determined by the size and shape of the entrance slit and was approximately 2 millimeters high by 26 millimeters wide. Most of the light from the plasma came from inside a 54 millimeter plasma diameter centered on the magnetic axis. The vertical resolution of the optics was about 4 millimeters after allowance for beam divergence over this distance.

The monochromator, beam rotator, stop, and lens were rigidly secured to a table (fig. 3). The table was supported by a pivot and adjustable screw. With this arrangement, chords of the plasma at positions above and below the horizontal centerplane of the test section could be viewed. The distance of the chord from the centerline of the test section is designated y (fig. 3).

The grating monochromator employed an f/8.6 $\frac{1}{2}$ meter Ebert mounting with curved slits. The reciprocal linear dispersion was 1.6 nanometers per millimeter in first order. Detection was by means of a magnetically shielded photomultiplier with S 20 photocathode. The photomultiplier was cooled to about -30° C by means of cold air from a vortex tube.

Other Diagnostic Equipment

A neutral particle analyzer (ref. 10) was located on the magnetic midplane on the opposite side from the monochromator and was used to measure energy distribution and mass of charge-exchange neutrals from the plasma.

A floating electrical probe could be substituted for the neutral particle analyzer and was equipped for rapid traverse of the plasma.

THEORY OF CHARGE-EXCHANGE DOPPLER BROADENING

Line Shapes

In most charge-exchange collisions involving electron exchange, the velocity of the projectile is little affected by the collision (ref. 14). Consequently, for a charge-exchange process of the type

$$A_f^+ + B \rightarrow A_f^* + B^+ \tag{I}$$

where the projectile A^+ is a positive atomic ion, the target B is a neutral atom or molecule, A^* is an electronically excited charge-exchange neutral atom with the same nucleus as A^+, B^+ is B with one electron removed, and f indicates high velocity, a measurement of the A^+ temperature can be obtained by measuring the temperature of A^* provided the A^+ temperature is much greater than the temperature of B. In low density plasmas in crossed $\vec{\mathscr{E}}$ and $\vec{B}$ fields this assumption is ful-

filled. The temperature T_i of A^* can be obtained by studying the Doppler broadening of the charge-exchange component of one of its spectral lines.

The first step in investigating charge-exchange Doppler broadening is to obtain the line shape function F, which is proportional to the emission intensity at a specific wavelength for an optically thin line and is normalized so that

$$\int_{-\infty}^{\infty} F(\Lambda)d\Lambda = 1 \tag{1}$$

where Λ is the displacement from the line center in terms of wavelength. It is assumed that A^+ has a Maxwell-Boltzmann velocity distribution (the loss cone of the mirror device and ion drift are neglected, and the cyclotron motion of the ions about magnetic field lines has small effect on the distribution at a given point in space). It is shown in appendix B that

$$F = \frac{M^{1/2}c}{2^{3/2}\lambda_0} \frac{\int_{\gamma}^{\infty} \sigma_*(E)e^{-E/kT_i}E^{1/2} dE}{\int_{0}^{\infty} \sigma_*(E)e^{-E/kT_i}E \, dE} \tag{2}$$

where σ_* is the charge-exchange cross section, E is ion energy in the laboratory system, and the other symbols are given in the LIST OF SYMBOLS (appendix A). For the special case where the cross section σ_* is a constant, equation (2) becomes

$$F = \frac{c}{2^{3/2}\lambda_0}\sqrt{\frac{M}{kT_i}}\left(\sqrt{\frac{\gamma}{kT_i}} e^{-\gamma/kT_i} + \frac{\sqrt{\pi}}{2} \text{erfc}\sqrt{\frac{\gamma}{kT_i}}\right) \tag{3}$$

If σ_* varies as v^{-1}, equation (2) gives a Gaussian line shape function.

A comparison of the well known Gaussian-Doppler line shape (ref. 15) and charge-exchange shapes from equations (2) and (3) is given in figure 4 for He^+ at 3000 electron volts temperature. It can be seen that equations (2) and (3) give an appreciably wider line than the Gaussian-Doppler line shape. Also, the assumption of constant σ_* gives an appreciably different line shape than variable σ_*.

Second Moment Equations

A closed form solution for T_i may be obtained for the constant σ_* case if the Doppler broadening of the charge-exchange component of the spectral line is measured in terms of its second moment defined by

$$\left\langle \Lambda^2 \right\rangle \equiv \int_{-\infty}^{\infty} \Lambda^2 F \, d\Lambda \tag{4}$$

which is the average value of the square of the wavelength deviation of the line profile from its center. Use of the second moment also facilitates corrections to $\left\langle \Lambda^2 \right\rangle$ given in appendixes C and D.

It is shown in appendix B that if σ_* is constant

$$\left\langle \Lambda^2 \right\rangle_3 = \frac{4}{3} \frac{kT_i \lambda_0^2}{Mc^2} \tag{5}$$

where the subscript 3 indicates that $\left\langle \Lambda^2 \right\rangle$ has been corrected for magnetic splitting, fine structure, and monochromator slit function; all of which would otherwise cause errors in T_i. Equation (5) may be solved for T_i in closed form.

It is also shown in appendix B that for the general case

$$\left\langle \Lambda^2 \right\rangle_3 = \frac{2\lambda_0^2}{3Mc^2} \frac{\displaystyle\int_0^{\infty} \sigma_*(E) e^{-E/kT_i} E^2 \, dE}{\displaystyle\int_0^{\infty} \sigma_*(E) e^{-E/kT_i} E \, dE} \tag{6}$$

The corrections to $\left\langle \Lambda^2 \right\rangle$ for magnetic splitting, fine structure, and monochromator slit function are derived in appendixes C and D. Let us assume we obtain the apparent shape of the charge-exchange component of the line by scanning the line with a monochromator and subtracting out the narrow component of the line (not due to charge exchange) and any continuum or dark current. The apparent second moment $\left\langle \Lambda^2 \right\rangle_1$ can then be obtained with a digitizer attached to an electronic desk calculator (or, if necessary, with a digital computer). From equations (C11) and (D15)

$$\left\langle \Lambda^2 \right\rangle_3 = \left\langle \Lambda^2 \right\rangle_1 - \sum_{i=1}^{k} I_i (\lambda_{0i} - \lambda_0)^2 - \frac{W^2}{8 \ln 2} \tag{7}$$

where the second term on the right is the correction due to magnetic splitting and fine structure, and the last term on the right is the correction due to the monochromator slit function. After the apparent second moment has been corrected by equation (7), equation (5) or (6) may be used to find T_i (some such scheme as interpolation of a table of $\langle \Lambda^2 \rangle_3$ and T_i has to be used with equation (6)).

Selection of Spectral Lines

Lines in the visible or near ultraviolet regions are the most convenient experimentally. For hydrogen H_α at 656.3 nanometer is the strongest and has the least interference from H_2 lines. H_β at 486.1 nanometer is weaker and, under some conditions, has serious interference from as many as eight H_2 lines (ref. 10). For helium, the 587.6 and 667.8 nanometer lines were found to exhibit the strongest charge-exchange components.

Cross Sections

The selection of appropriate charge-exchange cross sections for use in equation (6) is simplified by two facts: (1) Because the cross section appears in both the numerator and denominator, only the shape is important — the absolute value is immaterial. (2) Below a certain projectile energy, when an ion collides with an atom, a collision complex is formed so that for identical nuclei the direct excitation and charge-exchange excitation cross sections are approximately equal. Hence, data on the sum of the two cross sections suffices. For He^+, this occurs below about 15 kiloelectron volts (ref. 16), while for H^+ it occurs below about 5 kiloelectron volts (ref. 17).

In a hydrogen plasma, if the background gas is preominately H_2, the following charge-exchange processes are important.

$$H_f^+ + H_2(1s\sigma^2) \rightarrow H_f(n = 3) + H_2^+(1s\sigma) \tag{II}$$

$$H_f^+ + H_2(1s\sigma^2) \rightarrow H_f(n = 4) + H_2^+(1s\sigma) \tag{III}$$
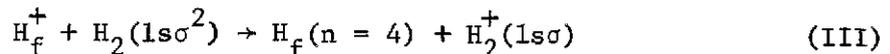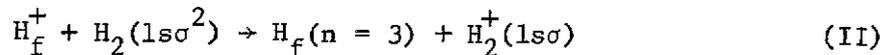
Optical cross sections have been measured by Hess (ref. 18) for the H_α and H_β lines generated predominantly by processes (II) and (III), respectively, for H^+ energies from 0.5 to 3 kiloelectron volts. These were extrapolated to lower energy by means of Massey's expression for the cross section of an inelastic atomic process (ref. 18). Hughes, Lin, and Hatfield (ref. 19) have measured these cross sections for H^+ energies from 5 to 130 kiloelectron volts. Hughes, et al. (ref. 20) have used experimental 3s, 3p, and 3d cross sections to synthesize improved H_α cross sections from 10 to 100 kiloelectron volts. It is impossible to

fair Hess's absolute cross sections into those of references 19 or 20 in a reasonable manner. Hess's work contains several possible experimental errors. Consequently, before fairing into cross sections from references 19 or 20, it was necessary to multiply all Hess's cross sections by a factor of 23.

In a hydrogen plasma if the background gas is appreciably dissociated, the following charge-exchange processes may be important.

$$H_f^+ + H(n = 1) \rightarrow H_f(n = 3) + H^+ \tag{IV}$$

$$H_f^+ + H(n = 1) \rightarrow H_f(n = 4) + H^+ \tag{V}$$
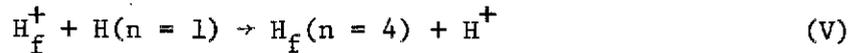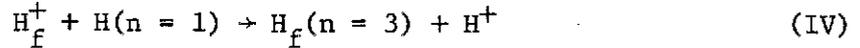
No experimental or theoretical cross sections are available for these processes. For estimates, the total cross section for the process

$$H_f^+ + H(n = 1) \rightarrow H_f(n = 2) + H^+ \tag{VI}$$
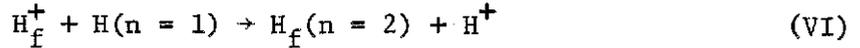
was obtained by adding the 2s and 2p cross sections of Bayfield (ref. 21) and Young (ref. 22), respectively. The sum was extrapolated to smaller energies by Massey's expression for the cross section of an inelastic atomic process (refs. 18 and 23) with the internal energy difference between the initial and final states $\Delta E = 10.20$ electron volts and the effective interaction range $a = 6.63 \times 10^{-8}$ centimeters. The 3s, 3p, 3d, 4s, 4p, and 4d cross sections were then estimated from the $n = 2$ cross section by assuming the n and ℓ dependence derived by May (ref. 24). The H_α optical cross section σ_α was then calculated from (ref. 20)

$$\sigma_\alpha = \sigma_{3s} + 0.1184 \, \sigma_{3p} + \sigma_{3d} \tag{8}$$

where the constant is a branching ratio. Similarly, the H_β optical cross section was calculated from

$$\sigma_\beta = 0.5842 \, \sigma_{4s} + 0.1190 \, \sigma_{4p} + 0.7456 \, \sigma_{4d} \tag{9}$$

where the three constants are branching ratios.

For helium the most important charge-exchange processes are

$$He_f^+ + He(1s^2 \, {}^1S) \rightarrow He_f(3d \, {}^3D) + He^+ \tag{VII}$$

$$He_f^+ + He(1s^2 \, {}^1S) \rightarrow He_f(3d \, {}^1D) + He^+ \tag{VIII}$$
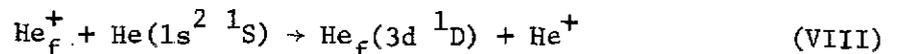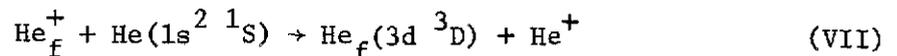
for the He 587.6 and 667.8 nanometer lines, respectively.

The cross section of process (VII) has been measured by Muller and
de Heer (ref. 25) between 1 and 150 kiloelectron volts. The total cross
section for direct excitation and charge-exchange excitation has been
measured by Dworetsky et al. (ref. 26) between 60 and 5000 electron volts
on a relative scale. For this report the two sets of cross sections were
normalized between 1 and 5 kiloelectron volts.

The cross section of process (VIII) has been measured by Muller and
de Heer (ref. 25) between 8 and 150 kiloelectron volts. The total cross
section has been measured by Dworetsky et al. (ref. 26) between 60 and
5000 electron volts on a relative scale. This leaves a region from 5 to
8 kiloelectorn volts that has not been measured. More recent work by
Tolk (ref. 27) disclosed that at 4 kiloelectron volts the total cross
section for the He 667.8 nanometer line was 0.491 times the total cross
section for the He 587.6 nanometer line. Hence, the Dworetsky, et al.
(ref. 26) relative cross sections for the 667.8 nanometer line were mul-
tiplied by 27×10^{-20} before fairing them into the charge-exchange cross
sections of Muller and de Heer (ref. 25).

Calculated Second Moments

Second moments were calculated by equation (6) using cross sections
from the previous section and lower and upper limits of integration of
theoretical threshold and 1 megaelectron volt, respectively. The results
are given in table I for the two best lines, assuming an H_2 background
gas for H_α. The results for H_α in table I were based on the high-energy
cross sections of Hughes, et al. (ref. 20), but did not change appreci-
ably below a temperature of 1 kiloelectron volt (the region of interest
in this report), when the cross sections of Hughes, Lin, and Hatfield
(ref. 19) were substituted.

Second moment calculations for H_α were also performed assuming an H
background gas. As can be seen from figure 5, the assumption of an H or
H_2 background gas had little effect on the calculated temperature for a
given value of second moment. However, in view of the estimated cross
sections for processes (IV) and (V), this conclusion should be considered
tentative.

RESULTS AND DISCUSSION

Test Conditions

The principal plasma parameters were the midplane magnetic flux
density, mirror ratio, total current for both sets of electrodes in par-
allel, electrode voltage, and gas pressure. The midplane magnetic flux
density was varied from 1.06 to 2.49 tesla. The mirror ratio varied from
1.52 to 1.57.

Conditions for hydrogen. - Total current amounted to 0.60 to 1.15 ampere. Electrode voltage was 7.0 to 20.4 kilovolts. Gas pressure was 6.7×10^{-5} to 1.12×10^{-4} torr.

Conditions for helium. - Total current was 0.45 to 1.05 ampere. Electrode voltage was 4.9 to 19.9 kilovolts. Gas pressure was 1.04×10^{-4} to 2.02×10^{-4} torr.

Conditions for mixture. - The mixture, which was used to obtain electron temperatures in hydrogen, consisted of 90 percent H_2 and 10 percent He by volume. Total current was 0.84 to 0.86 ampere. Electrode voltage was 11.9 to 18.8 kilovolts. Gas pressure was 1.13 to 1.24×10^{-4} torr.

Ion Temperatures

H^+ ion temperature. - A typical recording of the H_α line is shown in figure 6 for $y = 0$. The narrow central peak was caused by Franck-Condon neutrals and electron excitation of other neutrals and is of no interest. Since it had an approximately Gaussian line profile, it was easily faired out as shown. In some runs the H_2 657.2 nanometer line appeared (fig. 6). This was also faired out. The remaining curve was used to find the apparent second moment. The H_β line was similar.

Equations (7) and a more extensive version of table I were used to find ion temperatures from the H_α and H_β lines. The sum of the second moment corrections for magnetic splitting, fine structure, and monochromator slit function never exceeded 11 percent. In general, the temperatures derived from H_α and H_β, assuming H_2 background gas, were not exactly the same for $y = 0$ at identical experimental conditions, as figure 7 shows. On the average, H_β gave temperatures that were 71 percent of those obtained from H_α. This is in contrast to the deuterium results of Alexeff et al. (ref. 2) who found that D_α and D_β gave essentially the same ion temperatures. The cause of the discrepancy is not known, but calculations are in progress to see if the two-step process,

$$e_f + H(n = 1) \rightarrow e + H(n = 4) \tag{IX}$$

$$H_f^+ + H(n = 4) \rightarrow H_f(n = 4) + H^+ \tag{X}$$
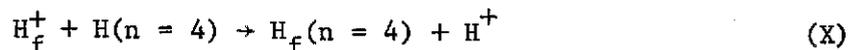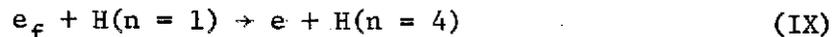
which should be significant at high H^+ densities, might be responsible. Process (X) is a resonant charge-exchange process in contrast to processes (II) to (V), which are nonresonant. This affects the energy dependence of the cross section, as shown in figure 8. Moreover, the cross sections for processes such as (X) scale as n^3 (ref. 28), whereas the cross sections for processes such as (II) to (V) scale as $1/n^3$ (ref. 17). Thus, it appears plausible that for H_β at sufficiently high ion densities, process (X) might predominate over processes (III) and (V), but for the same conditions processes (II) and (IV) might predominate for H_α. This would make the H_β charge-exchange component narrower than if proc-

esses (III) and (V) predominated (see fig. 8).

Process (X) is not the only possible explanation for the discrepancy between H_α and H_β temperatures. We have not considered the charge-exchange processes (refs. 2 and 18)

$$H_{2f}^+(1s\sigma) + H_2(1s\sigma^2) \rightarrow H_f(n) + H(n') + H_2^+ \qquad (XI)$$

$$H_f^+ + H_2^+(1s\sigma) \rightarrow H_f(n) + 2H^+ \qquad (XII)$$
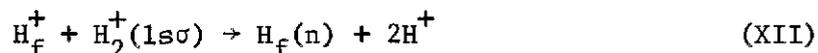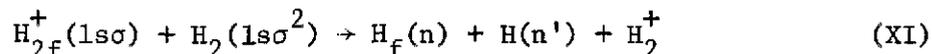
However, for process (XI), the cross sections for H_α and H_β have about the same energy dependence (ref. 18) and scale as $1/n^b$, where b is greater than 3. If the ion density were high enough, process (XII) might be important. Setting up to measure the electron density in SUMMA is in progress.

Another possible cause of the discrepancy between H_α and H_β is the longer radiative lifetimes of the $n = 4$ states of H. This would allow the $n = 4$ charge-exchange neutrals to travel further and, therefore, spread out more before radiating. The fast charge-exchange neutrals would spread out further than the slow ones, so H_β would appear narrower than for a homogeneous plasma. However, the effect should be more pronounced at high ion temperatures, which is not the case (see fig. 7).

The experimental results are averages across a plasma diameter. It would be more convincing if they could be Abel inverted to give ion temperature as a function of radius. However, at a specific wavelength, the radiation at a point is not isotropic due to the Doppler effect, so it does not appear that an Abel inversion is applicable at individual wavelengths.

Two correlations were used to relate ion temperature to plasma parameters for $y = 0$. In figure 9, H^+ temperature derived from H_α, assuming H_2 background gas, is plotted against the ratio of power input to magnetic flux density. Less scatter is obtained if H^+ temperature is plotted against power input divided by pressure and magnetic flux density, as shown in figure 10.

A paired comparison of H^+ temperatures derived from H_α and from a neutral particle analyzer is shown in figure 11. Each pair of temperatures were taken at the same time for the same plasma volume. The data are for $y = 0$, and the background gas was assumed to be H_2. The agreement is satisfactory.

He^+ ion temperature. - A typical recording of the He 587.6 nanometer line is shown in figure 12. The He 667.8 nanometer line was similar. The sum of the second moment corrections for magnetic splitting, fine structure, and monochromator slit function never exceeded 10 percent.

In general, the ion temperatures derived from the He 667.8 and 587.6 nanometer lines were not exactly the same for $y = 0$ at identical experimental conditions, as figure 13 shows. On the average, the He 667.8 nanometer line gave ion temperatures that were 65 percent of those from the 587.6 nanometer line. This may be due to the cross sections used. When He 587.6 nanometer charge-exchange cross sections were used for both lines, the temperatures agreed to within 3 percent. It will be recalled that the shape of the low-energy charge-exchange cross sections for both lines was obtained based on the assumption that the charge-exchange and direct excitation cross sections were equal. This may not be sufficiently accurate. Also, no cross sections for the He 667.8 nanometer line were available between 5 and 8 kiloelectron volts and so were estimated.

A more likely explanation for the lower ion temperatures from the He 667.8 nanometer line is obtained by considering the two-step processes

$$\begin{cases} He_f^+ + He \rightarrow He_f + He^+ & \text{(XIII)} \\[2em] e_f + He_f \rightarrow e + He_f^* & \text{(XIV)} \end{cases}$$

$$\begin{cases} e_f + He \rightarrow e + He^* & \text{(XV)} \\[2em] He_f^+ + He^* \rightarrow He_f^* + He^+ & \text{(XVI)} \end{cases}$$
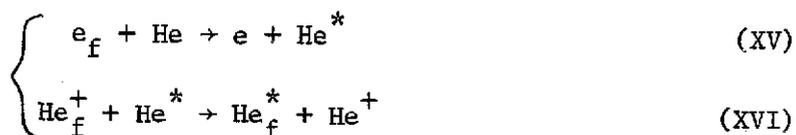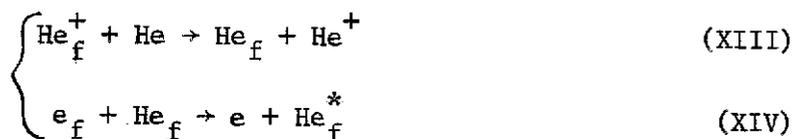
Order of magnitude calculations indicate that these processes are somewhat less important than processes (VII) and (VIII), and they cannot be included rigorously without knowledge of the free electron density and the geometry of the plasma. However, a conclusion may be drawn by examining the cross sections of processes (VII), (VIII), and (XIII) to (XVI). Process (VIII) has about half the cross section of process (VII) for typical energies, but processes (XIV) and (XV) have about the same cross sections for the He 587.6 and 667.8 nanometer lines. Process (XIII) is identical for both lines. There is no reason to believe that the cross sections for process (XVI) for the two lines are not essentially the same. Hence, processes (XIII) to (XVI) should contribute relatively more to the 667.8 nanometer line than to the 587.6 nanometer line. Since processes (XIII) and (XVI) are resonant, they would make the 667.8 nanometer line narrower (see fig. 8) and, if neglected, cause too low a temperature to be inferred.

The discrepancy in ion temperatures cannot be explained as a radiative lifetime effect because the radiative lifetimes of the upper states of the two lines are essentially the same.

Two correlations of ion temperature with plasma parameters were made. In figure 14, ion temperature for $y = 0$ is plotted against ratio of power input to magnetic flux density. Less scatter occurs in figure 15,

where ion temperature is plotted against power input divided by pressure and magnetic flux density.

A paired comparison of ion temperatures from the He 587.6 nanometer line and from a neutral particle analyzer is made in figure 16. The cause of the discrepancy is unknown.

Overview. – The measurement of ion temperature from the charge-exchange component of neutral atomic lines was found to be a simple procedure allowing direct data reduction with a minimum of assumptions. It does not disturb the plasma. The temperatures so obtained are in reasonable agreement with temperatures measured with a neutral particle analyzer. Accuracy can be improved by better models, more accurate cross sections, and inclusion of additional charge-exchange processes.

A comparison of ion temperatures obtained rigorously (eqs. (6) and (7)) with ion temperatures that would be obtained by erroneously applying the usual Gaussian Doppler half-width equation (eq. 4-117 of ref. 15) is interesting. If the charge-exchange process has a constant cross section, the erroneously obtained temperatures will be 71 percent too high. If the cross section is a function of energy, the erroneously obtained temperatures will be roughly 50 to 240 percent too high for the plasmas of this report.

Ion Drift

If the guiding centers of the ions drift with a velocity component parallel to the line of sight, the entire charge-exchange component of a neutral atomic line will be shifted relative to the narrow central component because of the Doppler effect. This follows since the central component is due principally to electron collision excitation of neutral atoms, which are not expected to drift appreciably. Hence, the shift of the charge-exchange component gives an indication of the drift velocity of the ions.

Alexeff et al. (ref. 2) found that the observed shift also depended on the distances along the line of sight to the front and rear walls of their machine due to cascading and transit time effects. However, this spurious shift could be eliminated if the distances to the front and rear walls were equal. Shift measurements were made in SUMMA in hydrogen and helium, and no spurious shifts were observed despite unequal wall distances. This was presumably due to the large inside diameter of the test section, which allowed decay before the neutrals struck the walls.

Results of measurements of H_α wide-component shifts as a function of y are shown in figure 17. These shifts are some sort of average across a chord, so it is difficult to interpret them quantitatively. However, if the shifts are interpreted as due to $\vec{\mathscr{E}} \times \vec{B}/B^2$ drifts, then they are approximately consistent with floating probe voltage measurements and calculated $\vec{B}$ fields. Both diagnostics indicate that the $\mathscr{E}$ field reverses

direction at roughly 3 centimeters. Figure 2 shows the probable reason for this. Between the anode and cathode B field lines, $\vec{\mathcal{E}}$ points inward. However, B field lines tend to allow a "short" between the cathode and the floating shield. The floating shield is then electrically connected by other B field lines to the region outside the anode B field lines. Hence, $\vec{\mathcal{E}}$ points outward from the anode B field lines. Thus, the plasma inside the anode B field lines rotates one direction and the plasma outside the anode B field lines rotates the other direction.

Similar shift results were obtained from the He 587.6 nanometer line.

Electron Temperature

The technique used for these measurements has already been reported (ref. 10). The method of relative intensity calibration was improved in the present work by using a larger tungsten strip lamp located on the centerline of the test section when in use and by taking into account the wavelength dependence of the correction for reflection from the lamp envelope.

To reduce the He line ratios to free electron temperatures, intensity ratios involving Maxwellian averages of optical cross sections are needed. The most reliable values for the 412.1, 443.8, 471.3, and 504.8 nanometer lines have been given by Latimer, Mills, and Day (ref. 7), although one must note that their "intensity ratios" are really ratios of numbers of photons emitted. For the He 706.5 and 728.1 nanometer lines, cross sections have been given by Jobe and St. John (ref. 29) for low energies and by Moussa, de Heer, and Schutten (ref. 30) for high energies.

All the following results are chordal averages for $y = 0$ (see fig. 3).

Electron temperatures in He. - Ratios of He 412.1 and 443.8 nanometer line intensities were measured for a variety of conditions and used to determine the electron temperatures. The results are shown in figure 18 and are in good agreement with reference 10.

Ratios of He 504.7 and 471.3 nanometer line intensities were measured for three conditions. They yielded electron temperatures an average of 60 percent higher than the He 412.1 and 443.8 nanometer lines. This compares with 29 percent higher in reference 10 and 27 percent higher on the centerline in BURNOUT VI after an Abel inversion (ref. 31).

Ratios of He 728.1 and 706.5 nanometer line intensities were measured for three conditions. They gave electron temperatures from 22 to 33 eV, an average of 13 percent higher than the He 443.8 and 412.1 nanometer lines.

The disagreement of the temperatures from the various line ratios can be explained by applying Sovie's first criterion (table I of ref. 6)

to the singlet S depopulation rates using up-to-date cross sections (refs. 7, 29, and 30). This showed that there was appreciable depopulation of the n = 4 and n = 5 levels by electron collision deexcitation. Hence, the temperatures from the n = 3 lines (728.1 and 706.5 nm) are the most reliable (ref. 6).

Electron temperatures in a mixture. - It is impossible to obtain electron temperatures from H line ratios because the dependence of their excitation cross sections on electron energy is too nearly the same. Consequently, 10 percent He was added to the hydrogen. Only four suitable He lines were sufficiently strong: 471.3, 504.8, 706.5, and 728.1 nanometers. Care was exercised to separate the He 471.3 and H_2 471.4 nanometer lines and also the He 728.1 and H_2 728.0 nanometer lines.

Electron temperatures were obtained from two ratios. Ratioing the 728.1 and 706.5 nanometer line intensities gave temperatures from 13.0 to 15.8 electron volts. These temperatures would fall well below the temperatures for pure helium if plotted in figure 18. This is what one would expect (ref. 32). Ratioing the 504.7 and 471.3 nanometer line intensities gave temperatures about 2.5 times as high.

The reason for the temperature discrepancy between the two pairs of lines is not the same as for pure helium. Applying Sovie's first criterion gave no evidence of depopulation of the singlet 4s level by electron collisions. Instead, we believe the reason for the discrepancy is depopulation of the upper state of the 471.3 nanometer line by collisions of the second kind.

$$He(4s \; ^3S) + H_{2f}^+(1s_\sigma) \rightarrow He(2p \; ^3P) + H(^2S) + H^+ \qquad (XVII)$$
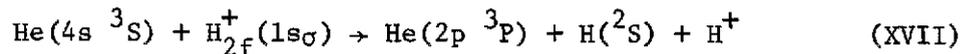
The dissociation energy for the ground vibrational state of H_2^+ is only 0.0208 electron volts more than the energy available when He drops from the $4s \; ^3S$ to the $2p \; ^3P$ state. Consequently, process (XVII) should have a large cross section (ref. 33). For deexcitation by process (XVII) to be just as important as radiative deexcitation, process (XVII) would have to have a cross section of 4.9×10^{-14} square centimeters for 10^{13} H_2^+ ions per cubic centimeter and an H_2^+ temperature of 1000 electron volts. This is a reasonable cross section if one considers the large orbital of the n = 4 state of He. A relatively large amount of H_2^+ at about this temperature has been observed in SUMMA with the neutral particle analyzer (ref. 10). The process analogous to process (XVII) but for singlet helium atoms would be expected to have a much smaller cross section because the energy deficit is 0.1951 electron volts instead of 0.0208 electron volts.

In view of the above discussion, electron temperatures from the 706.5 and 728.1 nanometer lines are more reliable. However, He 728.1 and H_2 728.0 nanometer lines are so close together that it might be more practical to use the He 706.5 and 504.8 nanometer lines to obtain electron temperatures in the future.

CONCLUDING REMARKS

Derivations are given which show that the determination of ion temperature from the charge-exchange component of a spectral line of a neutral atom can be put on a more quantitative basis if the second moment of the line profile is used as a measure of the ion temperature. Specifically, use of the second moment makes it feasible to take magnetic splitting, fine structure, monochromator slit function, and the energy dependence of the charge-exchange cross section into account. If one erroneously applies the usual Gaussian Doppler half-width equation to a charge-exchange line component with a constant charge-exchange cross section, the calculated temperature will be 71 percent too high. If the charge-exchange cross section varies, the similarly calculated temperature can easily be from 50 to 240 percent too high.

The results were applied to measurements of ion temperature in SUMMA. It was concluded that the Balmer α line and the He 587.6 nanometer line were most suitable for this application in hydrogen and helium plasmas, respectively. H^+ temperatures from 169 to 955 electron volts and He^+ temperatures from 666 to 5151 electron volts were obtained from these lines. In both plasmas, the ion temperature increased with the parameter P/pB, where P is power input, p is gas pressure, and B is magnetic flux density. Ion temperatures so derived are averages across the plasma and are believed accurate to within 30 percent for H^+ and 35 percent for He^+. This is substantiated by a paired comparison with neutral particle analyzer results obtained at the same time for the same plasma volume. It should be possible to improve this accuracy by the incorporation of more accurate charge-exchange cross sections, a more sophisticated plasma model, and additional charge-exchange processes.

Measurements of the shift of the charge-exchange component of a spectral line were also made. Results were approximately consistent with an $\vec{\mathcal{E}} \times \vec{B}/B^2$ drift velocity of the ions and indicated that the inner portion of the SUMMA plasma rotates one direction and the outer portion, the opposite direction. For more quantitative results, a more sophisticated plasma model is needed.

Electron temperatures were measured by the helium line ratio method assuming a corona model. Different line ratios gave somewhat different temperatures. The probable causes of this were diagnosed. It was concluded that the ratio of the He 706.5 and 728.1 nanometer lines gave the most reliable temperatures in pure He and in H_2-He mixtures. This ratio gave temperatures between 22 and 33 electron volts for helium and between 13 and 16 electron volts for a mixture of 90 percent hydrogen and 10 percent helium used to simulate pure hydrogen.

APPENDIX A

LIST OF SYMBOLS

A   constant in characteristic function, $Mc^2/2kT\lambda_0^2$

a   effective interaction range

$B,\vec{B}$ magnetic flux density

b   principal quantum number exponent for process (XI) cross section dependence

c   velocity of light

D   constant in characteristic function, $\dfrac{c}{\lambda_0}\sqrt{\dfrac{M}{2kT}}$

E   energy

ΔE internal energy difference between initial and final states

$\mathscr{E},\vec{\mathscr{E}}$ electric field

F   line shape function

F_e line shape function observed at exit slit

$_1F_1$ degenerate hypergeometric function

f   Maxwell-Boltzmann velocity distribution function

I_i integrated intensity of component i

k   Boltzmann's constant

ℓ azimuthal quantum number

M   mass of ion projectile

n,n' principal quantum numbers

P   power input to plasma

p   gas pressure

S   slit function of monochromator

T_i ion temperature

$v,\vec{v}$ absolute velocity

v_r	r-component of v
v_z	z-component of v
W	full half width at half intensity of S in wavelength units
x	difference between wavelength of light and monochromator setting, $\lambda - \lambda_m$
$\langle x^2 \rangle$	second moment of $S(x)$
y	distance from line of sight to centerline of test section (see fig. 3)
γ	wavelength difference parameter, $Mc^2\Lambda^2/2\lambda_0^2$
θ	polar angle
Λ	displacement from the center of the charge-exchange component of a spectral line, $\lambda - \lambda_0$
Λ_m	difference between wavelength set on monochromator and center of line, $\lambda_m - \lambda_0$
$\langle \Lambda^2 \rangle_1$	apparent second moment of charge-exchange component of spectral line
$\langle \Lambda^2 \rangle_2$	$\langle \Lambda^2 \rangle_1$ corrected for magnetic splitting and fine structure
$\langle \Lambda^2 \rangle_3$	$\langle \Lambda \rangle_2$ corrected for monochromator slit function
λ	wavelength of light
λ_m	monochromator setting
λ_0	wavelength of center of charge-exchange component of spectral line
λ_{0i}	wavelength of center of ith component due to splitting
σ_*	charge-exchange cross section for excitation to electronically excited state
$\sigma_\alpha, \sigma_\beta$	optical excitation cross sections
$\sigma_{3s}, \sigma_{3p}, \sigma_{3d}$ $\sigma_{4s}, \sigma_{4p}, \sigma_{4d}$	excitation cross sections for upper state given as subscript
Φ_F	characteristic function for F

Φ_S characteristic function for S

Φ_e characteristic function for F_e

ϕ azimuthal angle

ω Fourier transform argument

APPENDIX B

DERIVATIONS OF LINE SHAPES AND SECOND MOMENTS FOR DOPPLER-

BROADENED CHARGE-EXCHANGE NEUTRAL SPECTRA

We consider the charge-exchange reaction

$$A_f^+ + B \rightarrow A_f^* + B^+$$
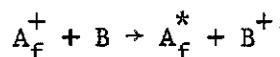
and assume A_f^+ has a Maxwell-Boltzmann velocity distribution and B is stationary. Davidson (ref. 34) has given the Maxwell-Boltzmann velocity distribution function f in polar coordinates.

$$f \, d\theta \, d\phi \, dv = \left(\frac{M}{2\pi kT}\right)^{3/2} e^{-Mv^2/2kT_i} v^2 \sin\theta \, d\theta \, d\phi \, dv \qquad (B1)$$

where θ and ϕ are the polar and azimuthal angles, respectively, between $\vec{v}$ and the line of sight, v is absolute velocity, M is the mass of A^+, and k is Boltzmann's constant. The probability of A_f^* having its velocity vector in $d\theta \, d\phi \, dv$ is directly proportional to f and directly proportional to $\sigma_*(v)v$, where $\sigma_*(v)$ is the charge-exchange cross section. Hence this probability is

$$\frac{\sigma_*(v)vf \, d\theta \, d\phi \, dv}{\int_0^\infty \int_0^{2\pi} \int_0^\pi \sigma_*(v)vf \, d\theta \, d\phi \, dv} \qquad (B2)$$

where the triple integral is required for renormalization. Combining equations (B1) and (B2) gives the probability as

$$\frac{\sigma_*(v)e^{-Mv^2/2kT_i} v^3 \sin\theta \, d\theta \, d\phi \, dv}{\int_0^\infty \int_0^{2\pi} \int_0^\pi \sigma_*(v)e^{-Mv^2/2kT_i} v^3 \sin\theta \, d\theta \, d\phi \, dv} \qquad (B3)$$

Equation (B3) is more tractable if the numerator is transformed from polar coordinates to cylindrical coordinates (v_z, ϕ, v_r), where both coordinate systems are shown in the following sketch.

Line of sight
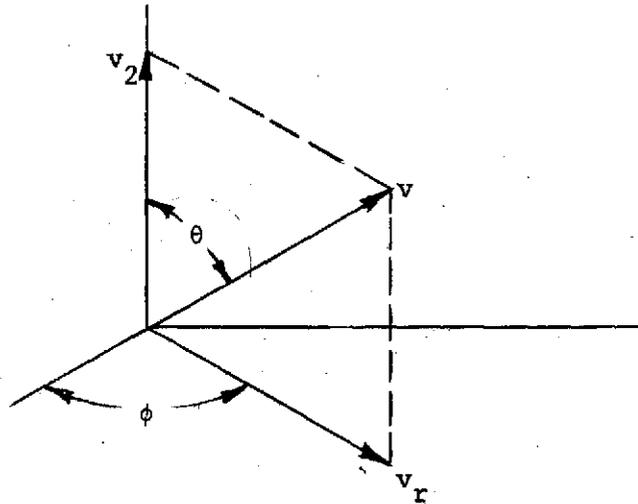
Making this transformation and integrating (B3) over all values of v_r and ϕ gives the probability of a charge-exchange neutral having v_z in dv_z as

$$\frac{\displaystyle\int_0^\infty \sigma_*\left(\sqrt{v_z^2 + v_r^2}\right) e^{-M(v_z^2+v_r^2)/2kT_i} \sqrt{v_z^2 + v_r^2}\; v_r \; dv_r \; dv_z}{\displaystyle\int_0^\infty \sigma_*(v) e^{-Mv^2/2kT_i} v^3 \, dv \int_0^\pi \sin\theta \, d\theta} \tag{B4}$$

Transforming the upper integral from v_r and v_z to v and v_z and evaluating the second integral in the denominator gives the probability for $v_z \geq 0$ as

$$\frac{\displaystyle\int_{v_z}^\infty \sigma_*(v) e^{-Mv^2/2kT_i} v^2 \, dv \, dv_z}{2\displaystyle\int_0^\infty \sigma_*(v) e^{-Mv^2/2kT_i} v^3 \, dv} \tag{B5}$$

We assume A^* emits a photon in a discrete transition. If we neglect the relativistic term in the Doppler relation (ref. 14) then

$$\Lambda = \frac{\lambda_0 v_z}{c} \tag{B6}$$

where λ_0 is the wavelength of the line center, c is the velocity of light, and Λ is the difference between the wavelength and λ_0. Converting equation (B5) from v_z to Λ and from v to energy E gives the probability

$$\frac{M^{1/2}c}{2^{3/2}\lambda_0} \frac{\displaystyle\int_\gamma^\infty \sigma_*(E)e^{-E/kT_i} E^{1/2} \, dE \, d\Lambda}{\displaystyle\int_0^\infty \sigma_*(E)e^{-E/kT_i} E \, dE} \tag{B7}$$

where

$$\gamma \equiv \frac{Mc^2\Lambda^2}{2\lambda_0^2} \tag{B8}$$

Since the line shape function is normalized to 1 (see eq. (1)), expression (B7) is equal to $F \, d\Lambda$. Although equation (B7) was derived for positive Λ, the same result is also obtained for negative Λ.

A special case of equation (B7) is obtained by letting σ_* be a constant. This gives

$$F \, d\Lambda = \frac{c}{2^{3/2}\lambda_0} \sqrt{\frac{M}{kT_i}} \left(\sqrt{\frac{\gamma}{kT_i}} \, e^{-\gamma/kT_i} + \frac{\sqrt{\pi}}{2} \, \text{erfc} \sqrt{\frac{\gamma}{kT_i}} \right) d\Lambda \tag{B9}$$

where erfc is the complementary error function. This is not the Gaussian profile usually encountered in Doppler broadening.

The second moments of the two line profiles can be obtained by substituting the respective F's into equation (4). For the $\sigma_*(E)$ case, equations (4) and (B7) give

$$\left\langle \Lambda^2 \right\rangle_3 = \frac{2\lambda_0^2}{3Mc^2} \frac{\displaystyle\int_0^\infty \sigma_*(E)e^{-E/kT_i} E^2 \, dE}{\displaystyle\int_0^\infty \sigma_*(E)e^{-E/kT_i} E \, dE} \tag{6}$$

If $\langle \Lambda^2 \rangle_3$ is known, T_i may be obtained from equation (6) by numerical methods. For the constant σ_* case equation (6) gives

$$\langle \Lambda^2 \rangle_3 = \frac{4}{3} \frac{kT_i \lambda_0^2}{Mc^2} \tag{5}$$

which gives T_i in closed form.

APPENDIX C

DERIVATION OF SECOND MOMENT CORRECTION DUE TO MAGNETIC

SPLITTING AND FINE STRUCTURE

In order to determine ion temperature from equation (5) or (6), two corrections should be made to the second moment $\langle \Lambda^2 \rangle_1$ of the charge-exchange neutral line observed by scanning with a monochromator. Because it is independent of the line shape, the first correction to make is the magnetic splitting and fine structure correction. A line may or may not have fine structure. It is well known that a magnetic field generally splits a fine structure component (or line if there is no fine structure) into several components. In mirror devices these components are usually sufficiently broadened that they overlap, especially for charge-exchange neutrals. This makes the observed line appear broader than it would otherwise appear and makes the observed second moment $\langle \Lambda^2 \rangle_1$ larger. The correction to $\langle \Lambda^2 \rangle_1$ derived below applies for any degree of component overlap, any type coupling in the atomic structure, and any strength magnetic field. However, it is assumed that the components have the same shape and second moment, although they will, in general, have different integrated intensities (the integrated intensity is the spectral light intensity of a component integrated over all wavelengths). We neglect polarization, although if the magnetic splitting correction ever were large compared to $\langle \Lambda^2 \rangle_1$ it would have to be taken into account (grating monochromators are notorious polarizers).

We assume each component has the same line shape function F normalized by

$$\int_0^\infty F(\lambda - \lambda_{0i}) d\lambda = 1 \qquad (C1)$$

where λ_{0i} is the wavelength of the center of the component. Also, each of the k components has an integrated intensity I_i normalized by

$$\sum_{i=1}^{k} I_i = 1 \qquad (C2)$$

where i specifies which component. The intensity of a component i at λ is proportional to $I_i F(\lambda - \lambda_{0i})$. The center of the k components collectively is

$$\lambda_0 = \frac{\displaystyle\int_0^\infty \lambda \sum_{i=1}^k I_i F(\lambda - \lambda_{0i})\,d\lambda}{\displaystyle\int_0^\infty \sum_{i=1}^k I_i F(\lambda - \lambda_{0i})\,d\lambda} \tag{C3}$$

Changing the order of integration and summation gives

$$\lambda_0 = \sum_{i=1}^k I_i \int_0^\infty \lambda F(\lambda - \lambda_{0i})\,d\lambda \tag{C4}$$

But

$$\int_0^\infty \lambda F(\lambda - \lambda_{0i})\,d\lambda \equiv \lambda_{0i} \tag{C5}$$

Combining equations (C4) and (C5) gives

$$\lambda_0 = \sum_{i=1}^k I_i \lambda_{0i} \tag{C6}$$

The observed second moment is

$$\langle \Lambda^2 \rangle_1 = \frac{\displaystyle\int_0^\infty (\lambda - \lambda_0)^2 \sum_{i=1}^k I_i F(\lambda - \lambda_{0i})\,d\lambda}{\displaystyle\int_0^\infty \sum_{i=1}^k I_i F(\lambda - \lambda_{0i})\,d\lambda} \tag{C7}$$

which can be rewritten

$$\langle \Lambda^2 \rangle_1 = \int_0^\infty \sum_{i=1}^k [(\lambda - \lambda_{0i}) + (\lambda_{0i} - \lambda_0)]^2 I_i F(\lambda - \lambda_{0i})\,d\lambda \tag{C8}$$

To simplify (C8) we define the second moment of component i by

$$\left\langle \Lambda^2 \right\rangle_2 \equiv \int_0^\infty (\lambda - \lambda_{0i})^2 \, F(\lambda - \lambda_{0i}) d\lambda \qquad (C9)$$

Since it has the same value for all k components, no subscript i is needed on $\left\langle \Lambda^2 \right\rangle_2$ (the 2 does not refer to a component). Combining equations (C8) and (C9) gives

$$\left\langle \Lambda^2 \right\rangle_1 = \left\langle \Lambda^2 \right\rangle_2 + \sum_{i=1}^{k} I_i (\lambda_{0i} - \lambda_0)^2 \qquad (C10)$$

Solving for $\left\langle \Lambda^2 \right\rangle_2$

$$\left\langle \Lambda^2 \right\rangle_2 = \left\langle \Lambda^2 \right\rangle_1 - \sum_{i=1}^{k} I_i (\lambda_{0i} - \lambda_0)^2 \qquad (C11)$$

For any atomic line the I_i's and the quantities $\lambda_{0i} - \lambda_0$ can be calculated in principle if the magnetic field strength, direction of observation relative to the magnetic field, and fine structure are known. For helium and hydrogen the only relevant cases are (1) Zeeman effect at low field strength, (2) intermediate coupling at intermediate field strength, and (3) Paschen-Back effect at high field strength.

After the fine structure has been removed from the line shape (corresponding to the use of eq. (C11)), the residual line shape may be assumed symmetrical about λ_0.

APPENDIX D

DERIVATION OF SECOND MOMENT CORRECTION DUE TO

SLIT FUNCTION OF MONOCHROMATOR

After making the correction for magnetic splitting and fine structure described in appendix C, the effect of the slit function of the monochromator (ref. 35) should be taken into account in the second moment. When a line is scanned with a monochromator, the line appears wider than it really is due to the finite width of the entrance and exit slits, optical aberrations, and unwanted diffraction. These effects are expressed collectively by the slit function of the monochromator, which is proportional to the response of the monochromator when set at one wavelength but illuminated by a different wavelength. Correcting for the slit function always reduces the second moment of a line shape.

We assume the slit function S and the line shape function F are symmetrical (any fine structure having been removed by application of equation (C11) to the second moment and a corresponding decomposition of the line shape function – although in practice the decomposition does not have to actually be carried out if only the temperature is desired). Let λ_m be the wavelength at which the monochromator is set and λ be the wavelength of some monochromatic light. We define

$$x \equiv \lambda - \lambda_m \tag{D1}$$

The slit function of many monochromators at medium to high resolution can be approximated by a Gaussian:

$$S(x) = \frac{2}{W} \sqrt{\frac{\ln 2}{\pi}} \, e^{-4x^2 \ln 2/W^2} \tag{D2}$$

where W is the full half width at half intensity in wavelength units and $S(x)$ is normalized by

$$\int_{-\infty}^{\infty} S(x)\,dx = 1 \tag{D3}$$

The second moment $\langle x^2 \rangle$ of $S(x)$ is

$$\langle x^2 \rangle = \frac{W^2}{8 \ln 2} \tag{D4}$$

Hence if W is measured experimentally, the second moment can be found from equation (D4). The line shape function F_e observed at the exit slit as the spectrum is scanned is obtained from Lincke (ref. 35) after

considerable manipulation.

$$F_e(\lambda_m - \lambda_0) = \int_0^\infty F(\lambda - \lambda_0) S(\lambda - \lambda_m) d\lambda \qquad (D5)$$

where $F(\lambda)$ is the true line shape function of the line incident upon the entrance slit. Because $S(\lambda - \lambda_m) = S(\lambda_m - \lambda)$ equation (D5) can be re-written

$$F_e(\Lambda_m) = \int_{-\infty}^\infty F(\Lambda) S(\Lambda_m - \Lambda) d\Lambda \qquad (D6)$$

where

$$\Lambda_m \equiv \lambda_m - \lambda_0 \qquad (D7)$$

which agrees with Griem (ref. 15). Mathematically F_0 is simply the convolution of F and S. According to Papoulis (ref. 36), the characteristic function $\Phi_e(\omega)$ of F_e is given by

$$\Phi_e(\omega) = \Phi_F(\omega) \Phi_s(\omega) \qquad (D8)$$

where $\Phi_F(\omega)$ and $\Phi_s(\omega)$ are the characteristic functions of F and S, respectively. The second moment (or variance) $\langle \Lambda^2 \rangle_2$ of F_e is then (ref. 36)

$$\langle \Lambda^2 \rangle_2 = -\left(\frac{d^2 \Phi_e}{d\omega^2} \right)_0 \qquad (D9)$$

where in identifying $\langle \Lambda^2 \rangle_2$ with F_e we have assumed that the line incident on the entrance slit has had the splitting removed from it (appendix C).

The characteristic function of F can be found from equation (B10) and is

$$\Phi_F(\omega) = \frac{1}{2} - \frac{\omega^2}{4A} {}_1F_1\left(1; \frac{3}{2}; -\frac{\omega^2}{4A}\right) + \frac{1}{2} {}_1F_1\left(1; \frac{3}{2}; -\frac{\omega^2}{4D^2}\right) \qquad (D10)$$

where ${}_1F_1$ is a degenerate hypergeometric function (ref. 37) and

$$A \equiv \frac{Mc^2}{2kT\lambda_0^2} \tag{D11}$$

$$D \equiv \frac{c}{\lambda_0} \sqrt{\frac{M}{2kT}} \tag{D12}$$

From equations (D2) and (D4)

$$\Phi_S(\omega) = e^{-1/2\langle x^2 \rangle \omega^2} \tag{D13}$$

From equations (D9), (D10), and (D13) and reference 37

$$\left\langle \Lambda^2 \right\rangle_2 = \left\langle x^2 \right\rangle + \frac{1}{2A} + \frac{1}{6D^2} \tag{D14}$$

From equations (B12), (D4), (D11), (D12), and (D14)

$$\left\langle \Lambda^2 \right\rangle_3 = \left\langle \Lambda^2 \right\rangle_2 - \frac{W^2}{8 \ln 2} \tag{D15}$$

This is the same law that applies if both F and S are Gaussian.

REFERENCES

1. Hirose, A.; and Alexeff, I.: Electrostatic Instabilities Driven by Currents Perpendicular to an External Magnetic Field, Nuc. Fusion, vol. 12, no. 3, May 1972, pp. 315-323.

2. Alexeff, I.; Guest, G. E.; McNally, J. R., Jr.; Neidigh, R. V.; and Scott, F. R.: Doppler-Broadened Spectral Emission from the Turbulently Heated Plasma of Burnout V. Phys. Rev. Ltrs., vol. 23, no. 6, Aug. 1969, pp. 281-283.

3. Hess, W. R.: Optical Measurement of the Velocity Distribution of the Protons in a Hot Plasma Beam. Phys. Ltrs., vol. 34A, no. 7, Apr. 1971, pp. 367-368.

4. Sigman, Donald R.; and Reinmann, J. J.: Steady-State Hot-Ion Plasma Produced by Crossed Electric and Magnetic Fields. NASA TM X-2783, 1973.

5. Sovie, Ronald J.: Spectroscopic Determination of Electron Temperature and Percentage Ionization in a Helium Plasma. Phys. Fl., vol. 7, no. 4, Apr. 1964, pp. 613-614.

6. Sovie, R. J.: The Effects of Cascading and Metastable Atoms on the Determination of Electron Temperature from Relative Line Intensities in a Tenuous Helium Plasma. J. Quant. Spectrosc. Radiat. Transfer, vol. 8, no. 3, Mar. 1968, pp. 833-838.

7. Latimer, I. D.; Mills, J. I.; and Day, R. A.: Refinements in the Helium Line Ratio Technique for Electron Temperature Measurement and Its Application to the Precursor. J. Quant. Spectrosc. Radiat. Transfer, vol. 10, no. 6, June 1970, pp. 629-635.

8. Roth, J. Reece; Richardson, Richard W.; and Gerdin, Glenn A.: Initial Results from the NASA Lewis Bumpy Torus Experiment. Presented at the American Physical Society, Annual Meeting, Philadelphia, Pa., Oct. 30-Nov. 4, 1973.

9. Richardson, Richard W.: Spectroscopic Investigation of NASA Lewis Bumpy Torus Plasma. Bull. Amer. Phys. Soc., vol. 18, no. 10, Oct. 1973, abstract 6H13, p. 1353.

10. Reinmann, J. J.; Lauver, M. R.; Patch, R. W.; Posta, S. J.; Snyder, A.; and Englert, G. W.: Hot Ion Plasma Heating Experiments in SUMMA. Presented at the First Intern. Conf. on Plasma Physics, Knoxville, Tenn., May 15-17, 1974.

11. Reinmann, J. J.; Swanson, M. C.; Nichols, C. R.; Obloy, S. J.; Nagy, L. A.; and Brady, F. J.: NASA Superconducting Magnetic Mirror Facility. Presented at Fifth Symp. on Engineering Problems of Fusion Research, Princeton, N.J., Nov. 5-9, 1973.

12. Lucas, E. J.; Stekly, Z. J. J.; de Winter, T. A.; Laurence, J. C.; and Coles, W. D.: The Design and Operation of an 88-kG 20-In.-Bore Superconducting Magnet System. Advances in Cryogenic Engineering, vol. 15, K. D. Timmerhaus, ed., Plenum Press, 1970, pp. 167-177.

13. Laurence, J. C.; Coles, W. D.; Brown, G. V.; and Meyn, E. H.: Performance Tests of 51-Cm-Bore Superconductive Magnets for a Magnetic-Mirror Apparatus. Advances in Cryogenic Engineering, vol. 15, K. D. Timmerhaus, ed., Plenum Press, 1970, pp. 178-183.

14. Thomas, Edward W.: Excitation in Heavy Particle Collisions. Wiley-Interscience, 1972, pp. 7 and 60.

15. Griem, Hans R.: Plasma Spectroscopy, McGraw-Hill, 1964, p. 101.

16. De Heer, F. J.; Muller, L. W.; and Geballe, R.: Electron Capture into Excited States by Helium Ions Incident on Helium. Physica, vol. 31, no. 12, Dec. 1965, pp. 1745-1755.

17. Bayfield, James E.: Electron Transfer in Simple Atomic Collisions: Recent Theory, Experiment and Applications. Paper presented at the Fourth Intern. Conf. on Atomic Physics, Heidelberg, Germany, July 1974.

18. Hess, W. R.: Electron Capture into the $n = 3,4$ States of H by Low Energy H^+, H_2^+ Impact on Hydrogen Gas. Phys. Ltrs., vol. 41A, no. 1, Aug. 1972, pp. 66-68.

19. Hughes, R. H.; Lin, Sabrina; and Hatfield, L. L.: Balmer Emissions Induced by Proton Impact on Molecular Hydrogen. Phys. Rev., vol. 130, no. 6, June 1963, pp. 2318-2321.

20. Hughes, R. H.; Stigers, C. A.; Doughty, B. M.; and Stokes, E. D.: Electron Capture into the $n = 3$ States of H by Fast H^+ Impact on Gases. Phys. Rev. A, vol. 1, no. 5, May 1970, pp. 1424-1432.

21. Bayfield, James E.: Measurement of the Total Cross Section for Charge Transfer into the Metastable State H(2s) for Proton Collisions with Atomic Hydrogen. Phys. Rev., vol. 185, no. 1, Sept. 5, 1969, pp. 105-112.

22. Thomas, E. W.: Excitation in Heavy Particle Collisions. Wiley-Interscience, 1972, p. 99.

23. Massey, H. S. W.; and Burhop, E. H. S.: Electronic and Ionic Impact Phenomena. Oxford, Clarendon Press, 1952, p. 515.

24. May, Robert M.: Production of Highly Excited Neutral Atoms for Injection into Plasma Devices: II. Nuc. Fusion, vol. 4, no. 3, Sept. 1964, pp. 207-212.

25. Muller, L. Wolterbeek; and De Heer, F. J.: Electron Capture into Excited States by Helium Ions Incident on Noble Gases. Physica, vol. 48, no. 2, Aug. 1970, pp. 345-396.

26. Dworetsky, S.; Novick, R.; Smith, W. W.; and Tolk, N.: Gross Failure of the Conventional Adiabatic Criterion; Structure and Coherence in the Low-Energy Excitation of Helium Atoms by Helium Ions. Phys. Rev. Ltrs., vol. 18, no. 22, May 1967, pp. 939-941.

27. Tolk, N.: personal communication. Bell Telephone Laboratories, Murray Hill, N.J., Sept. 20, 1974.

28. Bates, D. R.; and Reid, R. H. G.: Resonant Charge Transfer Between Protons and Excited Hydrogen Atoms. I. Quantal Two-State Approximation. J. Phys. B (Atom. Molec. Phys.), vol. 2, series 2, no. 8, Aug. 1969, pp. 851-856.

29. Jobe, John D.; and St. John, Robert M.: Absolute Measurements of the $2\,^1P$ and $2\,^3P$ Electron Excitation Cross Sections of Helium Atoms. Phys. Rev., vol. 164, no. 1, Dec. 1967, pp. 117-121.

30. Moussa, H. R. Moustafa; De Heer, F. J.; and Schutten, J.: Excitation of Helium by 0.05-6 keV Electrons and Polarization of the Resulting Radiation. Physica, vol. 40, no. 4, Jan. 1969, pp. 517-549.

31. Thermonuclear Division. ORNL-4688, Oak Ridge National Lab., 1971, pp. 81-82.

32. Cobine, James D.: Gaseous Conductors, Theory and Engineering Applications. Dover Publications, Inc., 1958, p. 44.

33. Mitchell, Allan C. G.; and Zemansky, Mark W.: Resonance Radiation and Excited Atoms. University Press, 1961, pp. 71-87.

34. Davidson, Norman R.: Statistical Mechanics. McGraw-Hill, 1962, p. 156.

35. Lincke, R.: Vacuum Ultraviolet Spectroscopy. Chapt. 6 of Plasma Diagnostics by W. Lochte-Holtgreven, ed., North Holland Publ. Co., 1968, pp. 347-423.

36. Papoulis, Athanasios: Probability, Random Variables, and Stochastic Processes. McGraw-Hill Book Co., 1965, pp. 153-159.

37. Gradshteyn, I. S.; Ryzhik, I. M.; Geronimus, Yu. V.; and Tseytlin, M. Yu. (Alan Jeffrey, trans.): Table of Integrals, Series, and Products. 4th ed., Academic Press, 1965, pp. 480-1058.

TABLE I. - SECOND MOMENT OF CHARGE-EXCHANGE NEUTRAL

COMPONENT OF TWO LINES AS A FUNCTION

OF ION TEMPERATURE

Ion temperature, T_i, eV	Second moment, $\langle \Lambda^2 \rangle_3$, nm²	
	Hydrogen Balmer alpha (H_α) (a)	Helium 587.6 nm line
20	0.4429×10^{-1}	0.5817×10^{-2}
25	.5228	.6356
30	.5990	.6885
40	.7437	.7922
50	.8807	.8937
60	0.1012×10^{0}	0.9934
70	.1139	$.1092 \times 10^{-1}$
80	.1262	.1189
100	.1495	.1382
140	.1914	.1768
200	0.2450	0.2352
240	.2766	.2746
300	.3206	.3346
400	.3891	.4361
500	.4562	.5394
600	0.5243	0.6452
700	.5940	.7547
800	.6652	.8680
1 000	.8106	$.1104 \times 10^{0}$
1 400	$.1104 \times 10^{1}$	.1580
2 000	0.1539	0.2255
2 400	.1827	.2689
3 000	.2260	.3343
4 000	.2990	.4482
5 000	.3718	.5692
6 000	0.4424	0.6954
7 000	.5093	.8235
8 000	.5719	.9499
10 000	.6837	$.1190 \times 10^{1}$
14 000	.8631	.1604

[a] H_2 background gas assumed.
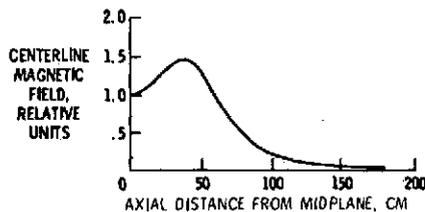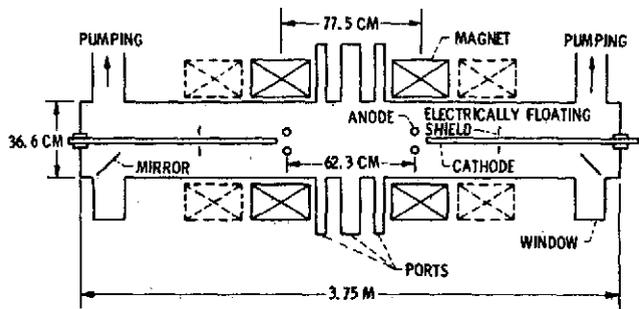
Figure 1. - Test section and magnetic field configuration.
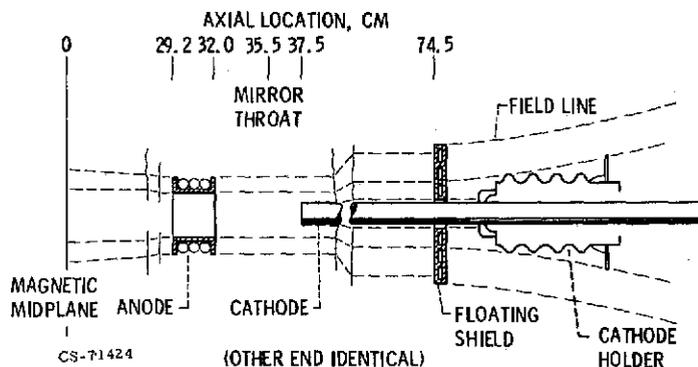
CS-69938

Figure 2. - Electrode configuration and magnetic field lines.
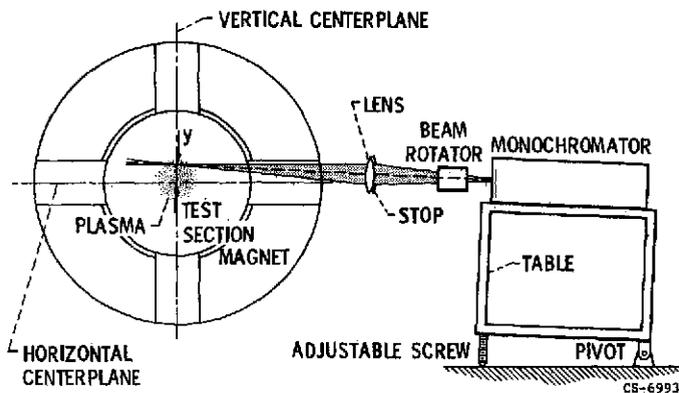
Figure 3. - Apparatus for Doppler broadening, shift, and line ratio measurements (not to scale).
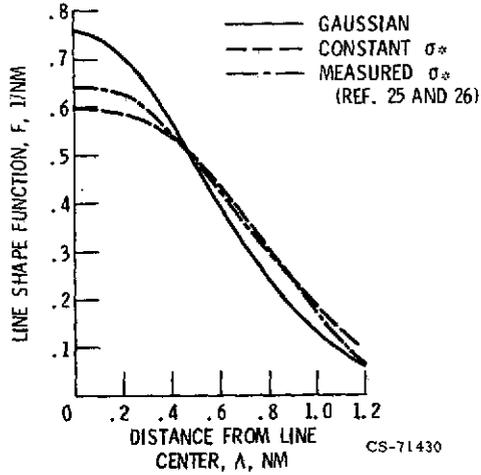
Figure 4. - Comparison of various He 587.6 nanometers line shapes for a He$^+$ temperature of 3000 electron volts.
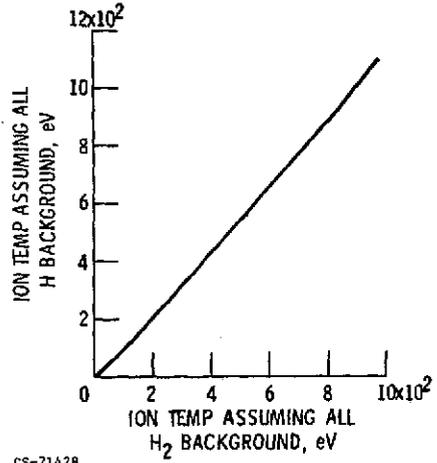
Figure 5. - Comparison of H$^+$ temperatures from H$_\alpha$ assuming different background gases.
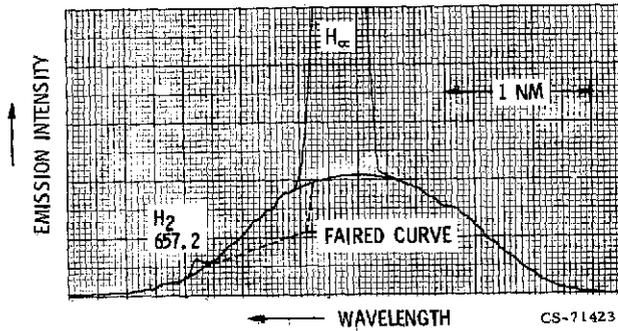
Figure 6. - Typical H$_\alpha$ line exhibiting wide and narrow components.
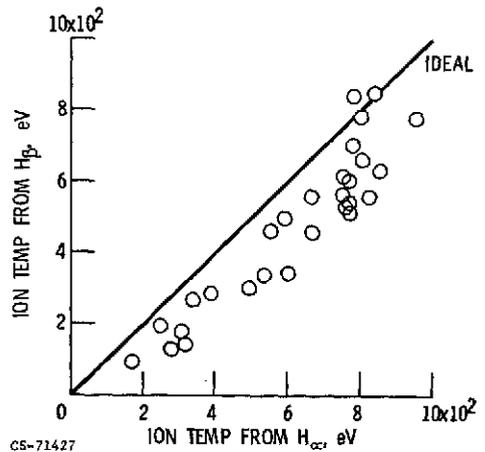
Figure 7. - Comparison of ion temperatures from H$_\alpha$ and H$_\beta$ assuming H$_2$ background.
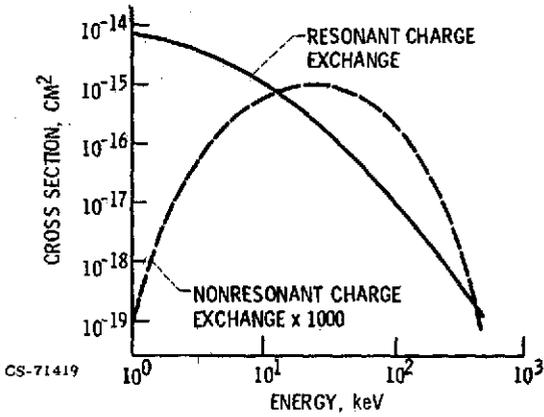
Figure 8. - Typical trends for resonant and nonresonant charge-exchange cross sections.

CS-71419

CS-71431
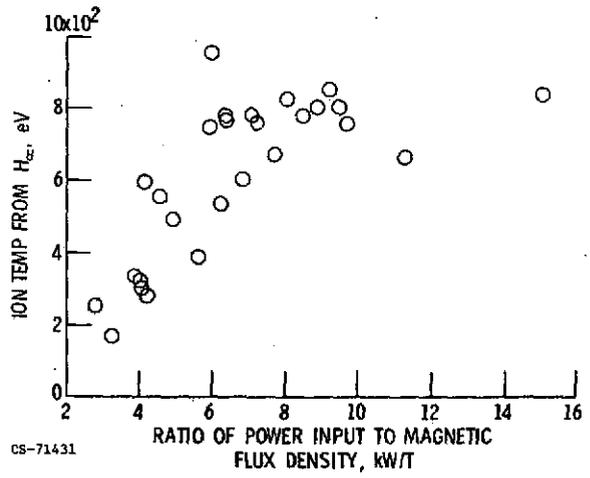
Figure 9. - H^+ ion temperature from H_α versus P/B.

CS-71434
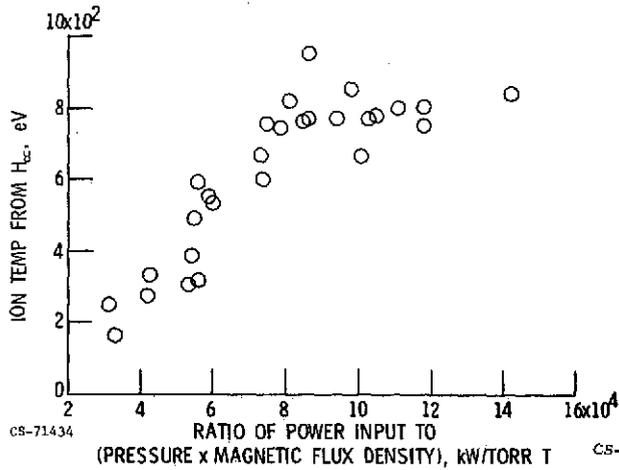
Figure 10. - H^+ ion temperature from H_α versus P/pB.

CS-71420
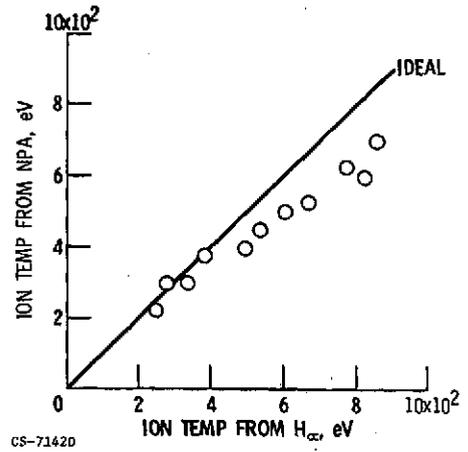
Figure 11. - Comparison of H^+ temperatures from H_α and from neutral particle analyzer.
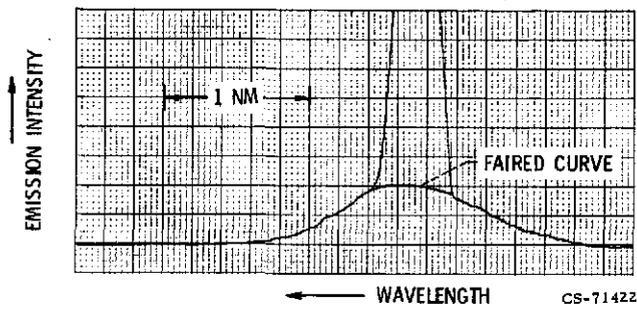
Figure 12. - Typical He 587.6 nanometer line exhibiting wide and narrow components.
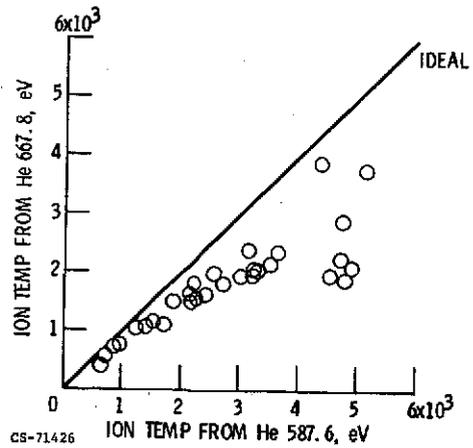
Figure 13. - Comparison of He$^+$ temperatures from He 587.6 and He 667.8 nanometer lines.
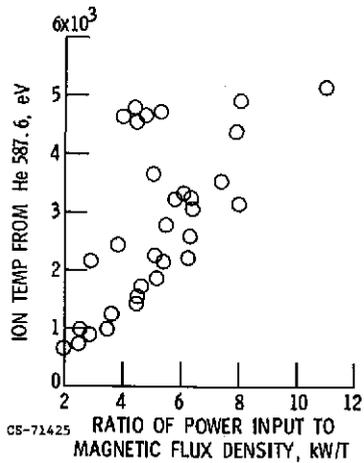
Figure 14. - He$^+$ ion temperature from He 587.6 versus P/B.
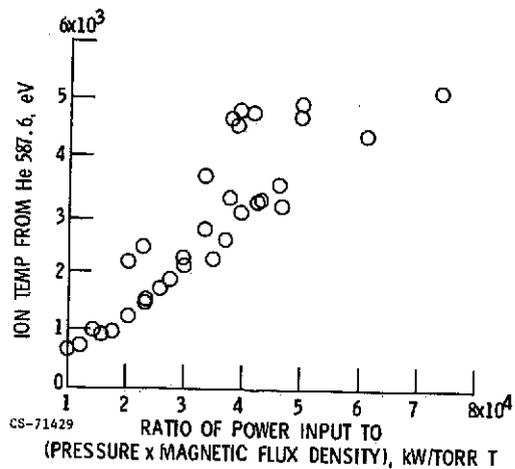

Figure 15. - He$^+$ ion temperature from He 587.6 versus P/pB.
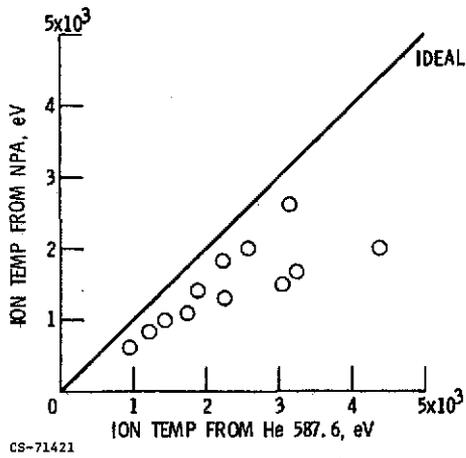
Figure 16. - Comparison of He$^+$ temperatures from He 587.6 nanometer line and from neutral particle analyzer.

CS-71421
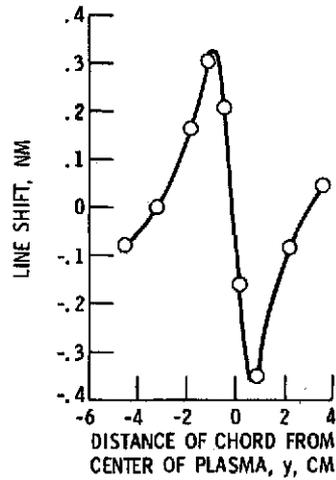
CS-71433

Figure 17. - Shift of wide component versus chord position for H$_\alpha$.
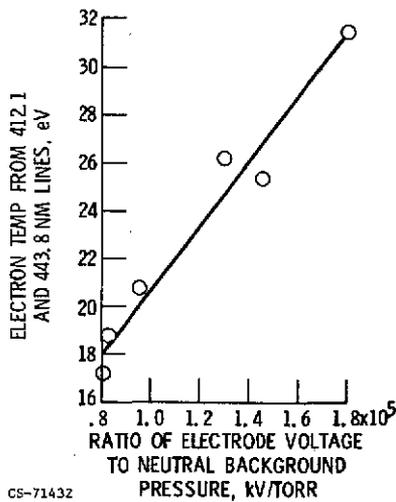
CS-71432

Figure 18. - Electron temperature versus ratio of electrode voltage to background pressure for He.

E-8169